Curved Glide-Reflection Symmetry Detection

Seungkyu Lee, *Member, IEEE,* and Yanxi Liu, *Senior Member, IEEE*

***Abstract*— We generalize the concept of bilateral reflection symmetry to curved glide-reflection symmetry in 2-dimensional Euclidean space, such that classic reflection symmetry becomes one of its six special cases. We propose a local feature-based approach for curved glide-reflection symmetry detection from real, unsegmented 2D images. Furthermore, we apply curved glide-reflection axis detection for curved reflection surface detection in 3D images. Our method discovers, groups and connects statistically dominant local glide-reflection axes in an Axis-Parameter-Space (APS) without pre-assumptions on the types of reflection symmetries. Quantitative evaluations and comparisons against state of the art algorithms on a diverse 64-test-image set and 1125 Swedish leaf-data images show a promising average detection rate of the proposed algorithm at 80% and 40% respectively, and superior performance over existing reflection symmetry detection algorithms. Potential applications in computer vision, particularly biomedical imaging, include saliency detection from unsegmented images and quantification of deviations from normality. We make our 64-test-image set publicly available.**

***Index Terms*— symmetry, glide-reflection, curved axis, curved surface.**

I. Introduction

SYMMETRY or approximate-symmetry is ubiquitous in the world around us and plays an important role in human and animal perception [1] [2] [3] [4] (Figure 1). Likewise, symmetry should play an important role for object description and recognition in computer vision [5]. An accurate automatic symmetry detection algorithm can aid many computer vision methods that perform pattern perception, object recognition and scene understanding. Among the four primitive symmetry types in 2D Euclidean geometry [6] (Figure 1): reflection, rotation, translation and glide-reflection, reflection symmetry (Figure 2 III, V, VI, VII) is one of the most commonly observed, analyzed and computationally treated primitive symmetries [6] [7] [5] (Table I). Reflection symmetry detection has been used in various applications, including face analysis [8], vehicle detection [9] [10] and medical image analysis [11] [12] [13].

Many real world symmetrical objects/patterns do not present a formally defined, rigid reflection symmetry that is associated with a straight reflection axis (e.g. Figure 2 VI)). Instead, they often follow either a *curved reflection* axis or a *glide-reflection* axis (Figure 2 right, Figure 1 bottom). A *glide-reflection symmetry* (Figure 2 II, V) is a primitive symmetry composed of a reflection and a translation along the direction of the reflection axis [6]. Except for the algorithm proposed in [14], which explicitly evaluates glide-reflection symmetries for specific wallpaper/frieze symmetry group classification, glide-reflection symmetry detection algorithms are rarely found in the computer vision literature. Detecting glide-reflection symmetry with a straight axis (Figure 1 (d)), a curved axis (Figure 1 bottom) in 2D, or curved glide reflection surface extraction in 3D (Figures 18 and 19) in general settings, has not been addressed computationally. An input image that has a curved glide reflection axis can be straightened to correspond to one of the 4 Frieze patterns [6] [14] that have horizontal reflection symmetries (Types II, V, VI and VII in Figure 2), and thus our proposed algorithm is also a first step towards detecting curved Frieze patterns in real images.

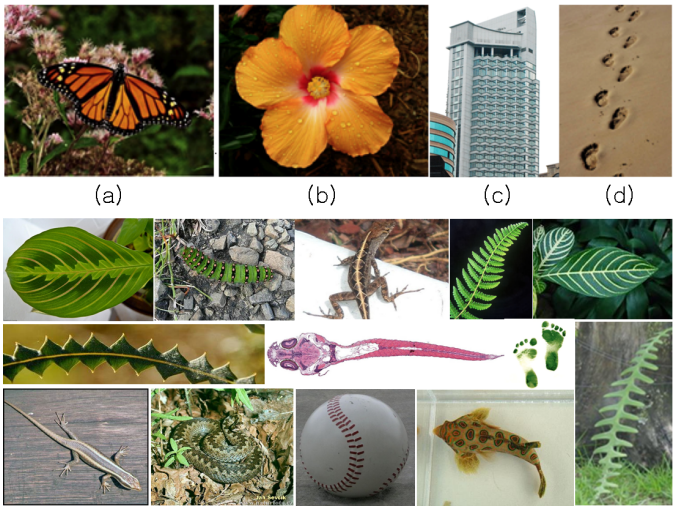

Fig. 1. Top: Examples of four different types of primitive symmetries [5] [6] in 2D Euclidean space: (a) Reflection (b) Rotation (c) Translation and (d) Glide-reflection. Bottom: The real world is full of curved reflection and glide-reflection symmetries.

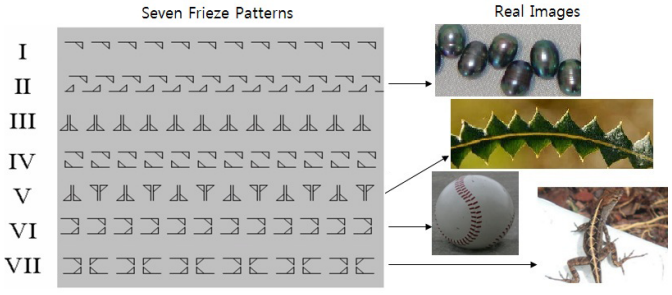

Fig. 2. Left: Seven distinct types of Frieze patterns [6]. Right: Real image samples related to the four frieze patterns that have reflection or glide-reflection symmetries.

The contributions of this paper include: (1) a conceptual and theoretical generalization of reflection symmetry to *curved glide-reflection symmetries* such that reflection symmetry, which has dominated the computer vision symmetry detection literature for the past 40 years, becomes one of six special cases of this generalization; (2) a novel curved glide-reflection symmetry axis detection algorithm for 2D unsegmented images and a direct application to curved reflection surface detection in 3D volumetric images; (3) a benchmark image set

(available with this publication) containing 64 real images for various types of glide reflection symmetries, and a quantitative evaluation and comparison of our proposed algorithm with the algorithms of Loy and Eklundh [15] and Peng et al. [16] on straight and curved reflection symmetry detection, respectively.

II. Related Work

Automatic detection of symmetry in natural and man-made objects has been a lasting research interest in computer vision, pattern recognition and robotics. The detection of reflection symmetry, in particular, has dominated the symmetry detection literature in computer vision (Table I). Since Birkoff and Kellogg [17]'s work in 1932, there has been a large and growing body of 2D/3D reflection symmetry detection algorithms proposed in the computer vision and computer graphics literature. These range from detecting Euclidean reflection symmetry [15], [20], [30], [31], [33], [37], [41], [42], [46], to affinely [18], [39] and perspectively distorted [22], [28], [29], [29], [34], [35], [38], [43], [45], [50] reflection symmetry.

In Euclidean space, Marola [20] introduces a planar reflection symmetry axis detection method. Tuzikov et al. [31] detect reflection symmetry axes from convex polygons based on Minkowski Addition. Sun and Si [37] detect reflection symmetry from a segmented gray image and its gradient information. These methods work on segmented or clean background images. On the other hand, there also are reflection symmetry detection methods working on unsegmented gray images. Kiryati and Gofman [33] detect globally maximal reflection symmetry from an unsegmented gray image based on a symmetry measure depending on the scale, orientation and distance of a supporting region. Yla-Jaaski and Ade [54] detect reflection symmetry of an object from its boundary edges. Prasad and Yegnanarayana [41] build gradient vector flow (GVF), a symmetry saliency map, and detect reflection symmetry. GVF was subsequently also used for rotation symmetry detection [55]. Yuan and Tang [42] find multiple reflection symmetries from a dilated and eroded edge measure. These algorithms detect symmetric objects without any skewing deformation. The first quantitative evaluation paper on discrete symmetry detection algorithms [56] finds a local feature-based method by Loy and Eklundh [15] as one of the best state of the art reflection symmetry detection algorithms from unsegmented images (detection rate on real multiple object images is 44%). In this paper, we compare our proposed algorithm with [15] on reflection symmetry with relatively straight reflection axes.

In 1981, Kanade coined the term *skewed symmetry* [18] to denote reflection symmetry of an object undergoing global affine or perspective skewing. Ponce [22] finds skewed reflection symmetry from object boundaries by characterizing Brooks ribbons. Algorithms developed by Carlsson [34], Lei and Wong [38], Van Gool et al. [29] and Shen et al. [39] detect reflection symmetry axes under perspective from segmented objects with clean backgrounds. Marola [43] proposes a perspective reflection symmetry axis detection method for synthetic and real gray images. Bitsakos et al. [50] propose a bilateral symmetry detection method from an object silhouette under perspective. Riklin Raviv et al. [52] propose perspective reflection and rotation symmetry extraction and segmentation methods. Milner et al. [57] focus on the symmetry detection of bifurcating structures like leaves. Sato and Tamura [30]'s method detects a planar or a curved 3D reflection symmetry from a contour shape with clean background. Recently, algorithms have been developed for partial or approximate Euclidean reflection symmetry detection in sub-sampled 3D data [46], and from un-segmented images directly [33] [15] [53]. Mitra et al. [49] propose a symmetrization method that straightens a curved reflection symmetry object based on locally straight reflection symmetries.

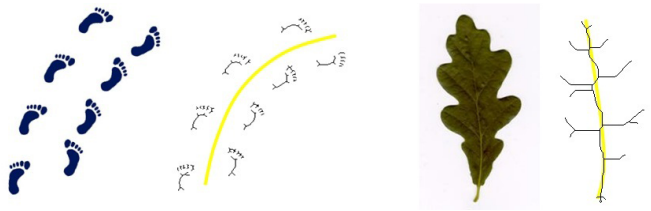

(A) (B)

Fig. 3. Results from a standard medial axis detection method [58] compared with those of the glide reflection axes (yellow curves) from our proposed algorithm : (A) Curved glide reflection symmetry can be extracted from a composition of multiple, disconnected objects, in this case without a continuous closed contour. (B) Even for an object with a closed contour, the texture pattern of the object, rather than its shape, dictates the dominant curved reflection symmetry axis, which differs from the output of the medial axis extraction algorithm on the same object.

Similar to a curved reflection symmetry axis, a *medial axis* is defined to be a topological skeleton of an object shape, usually derived from the object contour [59] [58]. The medial axis is composed of a set of centers of maximal inscribed disks of an object boundary. For a recent survey on medial axis, refer to [60]. Figure 3 illustrates the difference between the outcome of medial axis and curved glide reflection axis detection. Curved reflection symmetry can exist in a structure composed of multiple objects, such that they may not have a continuous closed contour (Figure 3 (a)). Even for an object with a closed contour, the medial axis may not always be consistent with the curved reflection symmetry axis of the texture pattern on an object (Figure 3 (b)). Peng et al. [16] work on the curved worm backbone detection and straightening problem, which is an application-specific, medial axis-based approach. They detect the medial axis from unsegmented input image based on intensity difference from the background. We compare the proposed method with this work in our experimental results, because the method can take an unsegmented image and the authors provide their source code. Levinshtein et al. [61] propose a partial medial axes detection algorithm for object recognition. Though the method [61] does not require a given closed contour, the object boundary obtained from the superpixel segmentation and grouping is necessary for the subsequent medial axis detection.

Mid-sagittal plane (MSP) detection from the 3D MR image of human brain is a 3D reflection symmetry plane detection problem. Guillemaud et al. [62] propose a MSP detection method from a set of 3D points by fitting a plane with minimum distance error to the points. Liu et al. [63] [64] [13] use a

TABLE I

REFLECTION SYMMETRY DETECTION ALGORITHMS IN THE LITERATURE

	A Glance of Reflection Symmetry Detection Algorithms				
	2D Euclidean		2D Skewed		3D Euclidean
	Segmented	Un-segmented	Segmented	Un-segmented	Segmented
1932	Birkoff & Kellogg [17]				
1983			Kanade [18]		
1985					Wolter et al. [19]
1989	Marola [20]				
1990	Marc and Medioni [21]			Ponce [22]	Liu [23]
1992		Zielke et al. [24]			
1993		Labonte et al. [25]			
1994					Liu and Popplestone [26]
1995	Zabrodsky et al. [27]		Mukherjee et al. [28]		
1996			Van Gool et al. [29]		Sato and Tamura [30]
1997	Tuzikov et al. [31]				Sun and Sherrah [32]
1998		Kiryati & Gofman [33]	Carlsson [34]	Curwen et al. [35]	
			Bruckstein and Snaked [36]		
1999	Sun and Si [37]		Lei & Wong [38]		
2000			Shen et al. [39]		
2002					Kazhdan et al [40]
2004		Prasad et al. [41]			
2005		Yuan & Tang [42]	Marola [43]		
		Liu et al. [44]			
2006		Loy & Eklundh [15]		Cornelius & Loy [45]	Mitra et al. [46]
					Martinet et al. [47]
					Podolak et al. [48]
2007					Mitra et al. [49]
2008			Bitsakos et al. [50]		Pauly et al. [51]
2009				Riklin Raviv et al. [52]	
2010				Liu and Liu [53]	

set of correlation maps from 2D slices to estimate the 3D ideal MSP of normal and pathological brains (where brains can be severely asymmetrical). Ardekani et al. [65] extract MSP based on cross correlation of two intensity vectors. Minoshima et al. [66] detect bilateral symmetry regions using stochastic sign change. Prima et al. [67] maximize the reflection symmetry measured by correlation for MSP detection. In all of these MSP detection methods, MSP is considered as a 2D planar surface. Some human brains show a clear bending along their mid-sagittal fissure. Stegmanna et al. [68] detect the curved mid-sagittal surface (MSS) by maximizing local symmetry at every 2D slice of the brain. However, the cross-correlation-based reflection symmetry detection in their algorithm is sensitive to irregular conditions, such as a brain tumor that pushes the MSP to form a non-planar surface.

III. CURVED GLIDE-REFLECTION FORMALIZATION

Glide-Reflection is defined in [6] as a symmetry that is composed of a translation T along and a reflection R about the same axis (Figure 1 (d), Figure 2 case II). A pair of image patches P_{i_1}, P_{i_2} has a *local glide-reflection* symmetry if and only if $P_{i_1} = T_i + R_i(P_{i_2})$ (Figure 4 (2)). When $T_i = 0$, $P_{i_1} = R_i(P_{i_2})$ is a pure reflection (Figure 4 (1)). Let C_i, short for C_{R_i,T_i}, represent a center point between image patches P_{i_1}, P_{i_2} (Figure 4).

We define a *Curved Glide-Reflection Symmetry* as: a sequential collection of local glide-reflection symmetries $[(T_1, R_1), ...(T_i, R_i), ...(T_n, R_n)]$ with corresponding image patch pairs $[(P_{11}, P_{12}), ..., (P_{i_1}, P_{i_2}), ..., (P_{n_1}, P_{n_2})]$ and associated center points $C = [C_1, C_2, ..., C_i, ..., C_n]$, such that a smooth curve $\mathcal{C}$ can be found that passes through all points in C sequentially and is tangent to each local reflection axis of R_i at C_i. The shortest such curve $\mathcal{C}_{\min}$ is defined to be the axis of the curved glide reflection symmetry.

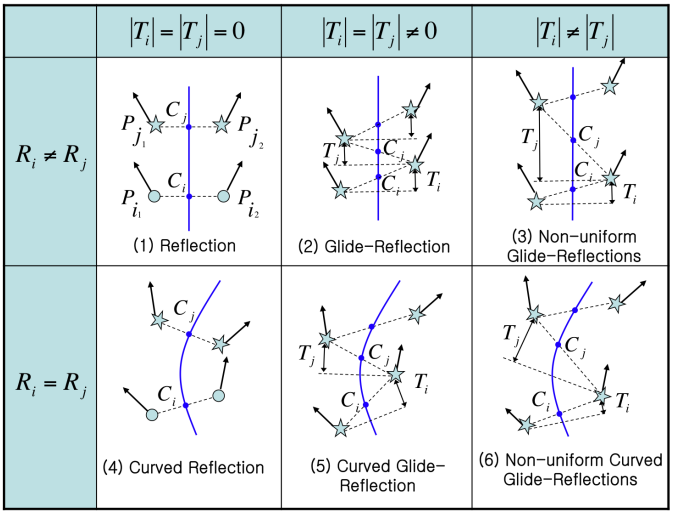

Fig. 4. The six special cases of curved glide-reflection symmetry. In (2),(3),(5),(6), only cases where patches $P_{i_2} = P_{j_1}$ are shown, though $P_{i_2} \neq P_{j_1}$ is also allowed.

Let C_i and C_j be two adjacent, nonidentical center points ($C_i \neq C_j$) in C. Then a curved glide-reflection symmetry can be categorized as follows:

- When $R_i = R_j$ (Straight reflection axis)
  (1) if $|T_i| = |T_j| = 0$, *Reflection* (Figure 4 (1)) ;
  (2) if $|T_i| = |T_j| \neq 0$, *Glide-Reflection* (Figure 4 (2)) ;
  (3) if $|T_i| \neq |T_j|$, *Non-Uniform Glide-Reflection* (Figure 4 (3));
- When $R_i \neq R_j$ (Curved reflection axis)
  (4) if $|T_i| = |T_j| = 0$, *Curved Reflection* (Figure 4 (4));
  (5) if $|T_i| = |T_j| \neq 0$, *Curved Glide Reflection* (Figure 4 (5));

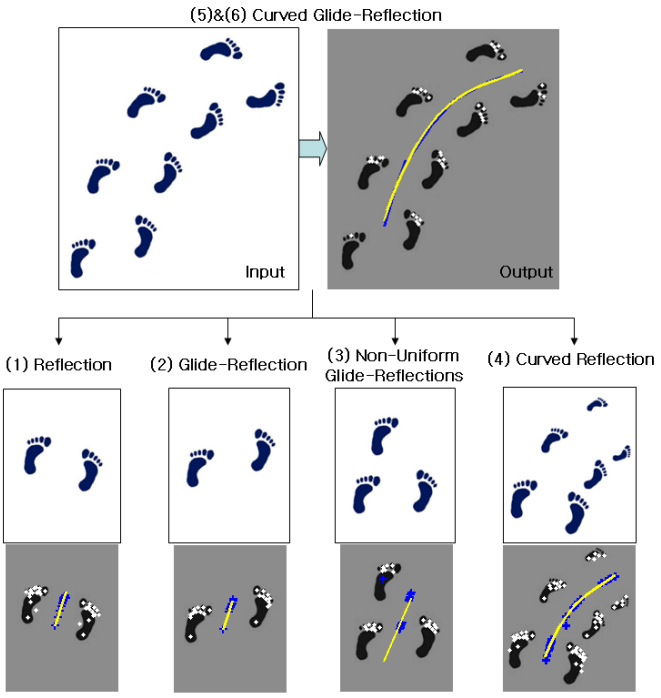

Fig. 5. Curved glide-reflection and its special cases. Curved glide-reflection includes the non-uniform glide reflection, i.e. cases (5) and (6) shown in Figure 4. Detected axes by the proposed algorithm (yellow lines) are shown. Blue dots are the center points of the supporting local feature pairs.

(6) if $|T_i| \neq |T_j|$, *Curved Non-Uniform Glide Reflection* (Figure 4 (6));

IV. Glide-Reflection Detection

We propose a local feature point-based matching method for glide-reflection symmetry detection. Figure 6 is a flowchart of our proposed curved glide-reflection symmetry detection algorithm. From a filtered input image, we collect matching point pairs and group them in a 3D axis parameter space (APS). A curve fitting method is applied to detect a global curved glide-reflection axis on each detected matching point pair group.

A. Feature Point Detection

Feature point-based matching [15] allows efficient correspondence detection by examining local oriented feature points rather than the whole input image. The set of available feature points is critical to our proposed algorithm performance. If only a small number of feature points are found from the input image, the cue to support a reflection symmetry may be missing or weak. To overcome this problem, we propose to use multiple image filters (gray, dilated edge and gradient image) before performing key point detection. In our experiments, we use SIFT [69] feature point matching. Though SIFT detects distinctive points robustly with good repeatability [15], SIFT key points are only detected at local maxima or minima locations, which are rare on an image with gradual change of intensity. Thus we also filter the image using gradient and Canny edge detectors. These filtered images give additional

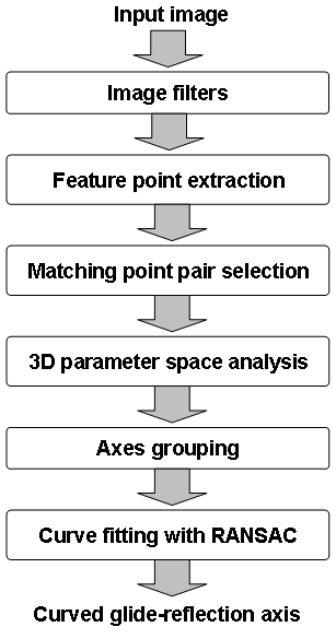

Fig. 6. Flowchart for the proposed curved glide-reflection symmetry detection algorithm.

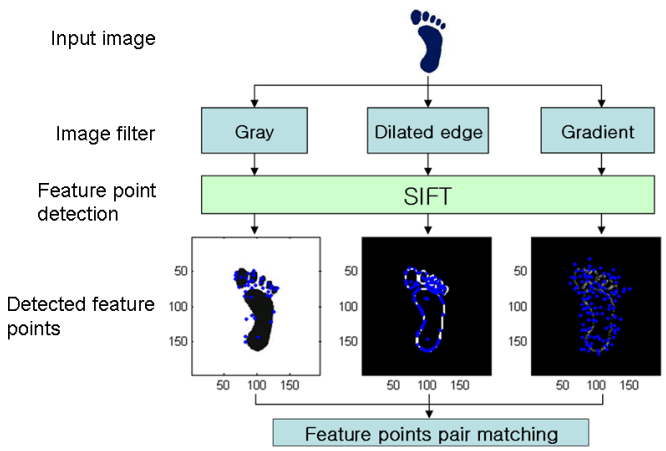

Fig. 7. Feature point detection from three different filtered input images

SIFT key points in local regions where key points were not detected in the original intensity image (Figure 7). As a result, we obtain more potential matching pairs for symmetry detection. Table III shows the effect of these image filters on glide-reflection symmetry detection performance.

B. Matching Pairs Selection

A feature point P_i is represented by its location x_i, y_i, orientation ϕ_i and scale s_i defined on the corresponding local patch of the feature point [69], i.e $P_i(x_i, y_i, \phi_i, s_i)$ [15]. Given a set of detected feature points, all possible pairs of feature points are analyzed to find the reflection symmetry R based on a set of local feature descriptors. The orientation of each reflection axis is computed from the orientations of a pair of matched points. The offset or translation T of a potential glide-reflection symmetry is found from the relative locations and orientations of matched feature point pairs (Figure 8).

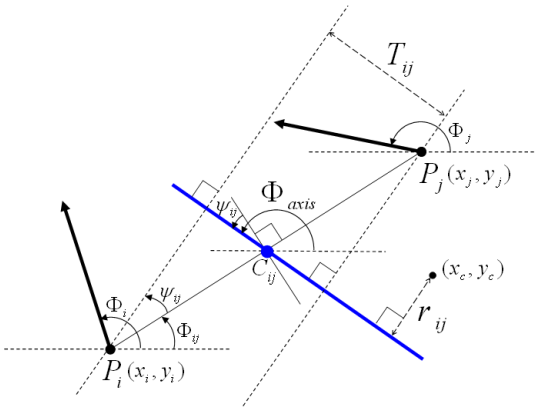

Fig. 8. The orientation of the glide-reflection axis ϕ_{axis} and translation T_{ij}

Given SIFT feature points and their local descriptor vectors, we compare all possible pairs of orientation-normalized feature points. If two orientation-normalized feature points exhibit a glide-reflection symmetry ($P_i = T + R(P_j)$), the descriptor vector of one point matches with the mirrored descriptor vector of the other point. Similarity for matching is quantified by the Euclidean distance between the SIFT descriptors. After we sort the pairs by their similarity score at each feature point, the top N matched pairs are chosen to be the candidate set. In our experiments, we use an empirical value of $N = 3$. In [15], glide-reflection pairs (Figure 5 (2)) are penalized. In our algorithm, we treat both glide-reflection ($T \neq 0$) and reflection ($T = 0$) symmetries uniformly while letting the transformation T value tell them apart.

Under our formulation, glide-reflection symmetries and pure reflection symmetries can be distinguished in a three-dimensional axis parameter space (APS) of glide-reflection axes, as shown below. Let $P_i = (x_i, y_i, \phi_i, s_i)$ and $P_j = (x_j, y_j, \phi_j, s_j)$ be two feature points (Figure 8) and C_{ij} be the center point between them. ϕ_i, ϕ_j and ϕ_{ij} are the orientation values of two key points and the line connecting them. If the two points of a matched pair form a glide-reflection symmetry, the orientation of its axis, ϕ_{axis}, is simply the average of the orientations of the two key points:

$$\phi_{axis} = \frac{\phi_i + \phi_j}{2} = \phi_{ij} + \psi_{ij} + \frac{\pi}{2} \quad (1)$$

where ψ_{ij} is the deviation angle of the glide-reflection axis from the perpendicular line to the line connecting the two points (P_i and P_j). Then the translation component T_{ij} of a potential glide-reflection axis can be calculated from the following equation:

$$T_{ij} = d_{ij} sin(\psi_{ij}) = d_{ij} sin(\frac{\phi_i + \phi_j - \pi}{2} - \phi_{ij}) \quad (2)$$

where, $d_{ij} = \sqrt{(x_i - x_j)^2 + (y_i - y_j)^2}$ is the distance between the two points. We also calculate the distance r_{ij} from the image center (x_c, y_c) to the glide-reflection axis:

$$r_{ij} = (\frac{x_i + x_j}{2} - x_c) sin\phi_{axis} - (\frac{y_i + y_j}{2} - y_c) cos\phi_{axis} \quad (3)$$

Now we can express our glide-reflection symmetry as $P_j = T_{ij} + R_{r_{ij},\phi_{axis}}(P_i)$, where $R_{r_{ij},\phi_{axis}}$ is the reflection mapping with respect to the reflection axis (r_{ij}, ϕ_{axis}) and T_{ij} is a translation offset. Thus, $(T_{ij}, r_{ij}, \phi_{axis})$ form a three dimensional APS for glide-reflection symmetries (Figure 9). We construct and analyze the distribution of the three glide-reflection axis parameters detected in real images. Each matched pair (P_i and P_j) point in the 3D APS is weighted by M_{ij}, a product of the scaling $S_{ij} = e^{(\frac{-|s_i - s_j|}{s_i + s_j})}$ and distance $D_{ij} = e^{(\frac{-d_{ij}^2}{2max(d_{ij})})}$ as follows [15]:

$$M_{ij} = S_{ij} \times D_{ij} = e^{(\frac{-|s_i - s_j|}{s_i + s_j})} \times e^{(\frac{-d_{ij}^2}{2max(d_{ij})})} \quad (4)$$

where d_{ij} is the distance and s_i and s_j are the scales of P_i and P_j.

Feature point pairs of similar size and shorter distance are given higher weight [15]. This 3D APS distribution is then convolved with a Gaussian kernel (we use empirical value $\sigma = 2.5$) to build a 3D density map. Local maximum points indicate dominant axes.

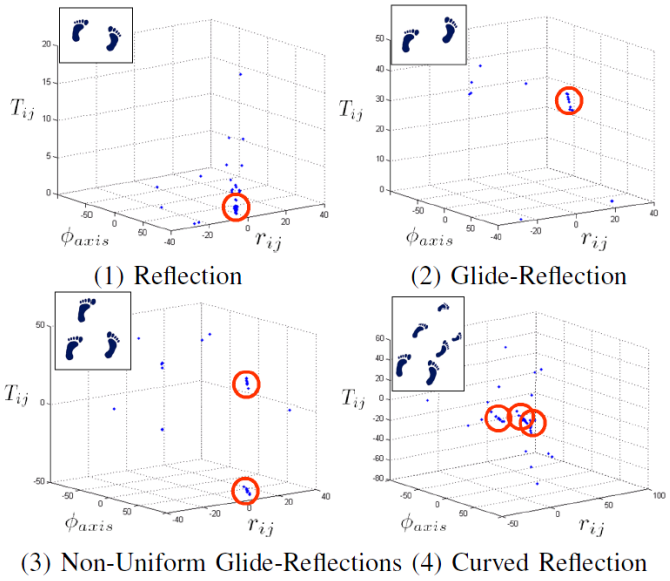

Fig. 9. 3D APS examples of the four special cases of curved glide-reflection symmetries: Red circles show the characteristic patterns detected in the 3D APS location.

Figure 9 shows votes in 3D APS space for four examples of curved glide-reflection symmetry. If the glide-reflection axis of the input image is straight, the voting in the 3D APS should be centered around a point-like local maxima when projected to (r_{ij}, ϕ_{axis}) (Figure 9 (1)). Reflection symmetry is detected near $T_{ij} = 0$ (red circle of Figure 9 (1)). Glide-reflection with a straight axis has a single non-zero T_{ij} value (red circle of Figure 9 (2)) while locally deformed glide-reflection has multiple (two or more) non-zero T_{ij} values (One is positive and the other is negative in Figure 9 (3)). In Figure 9 (4), three local maximum locations on the $T_{ij} = 0$ plane indicate the existence of a curved reflection axis. These special cases form the basic building blocks for a general curved glide-reflection symmetry detection algorithm.

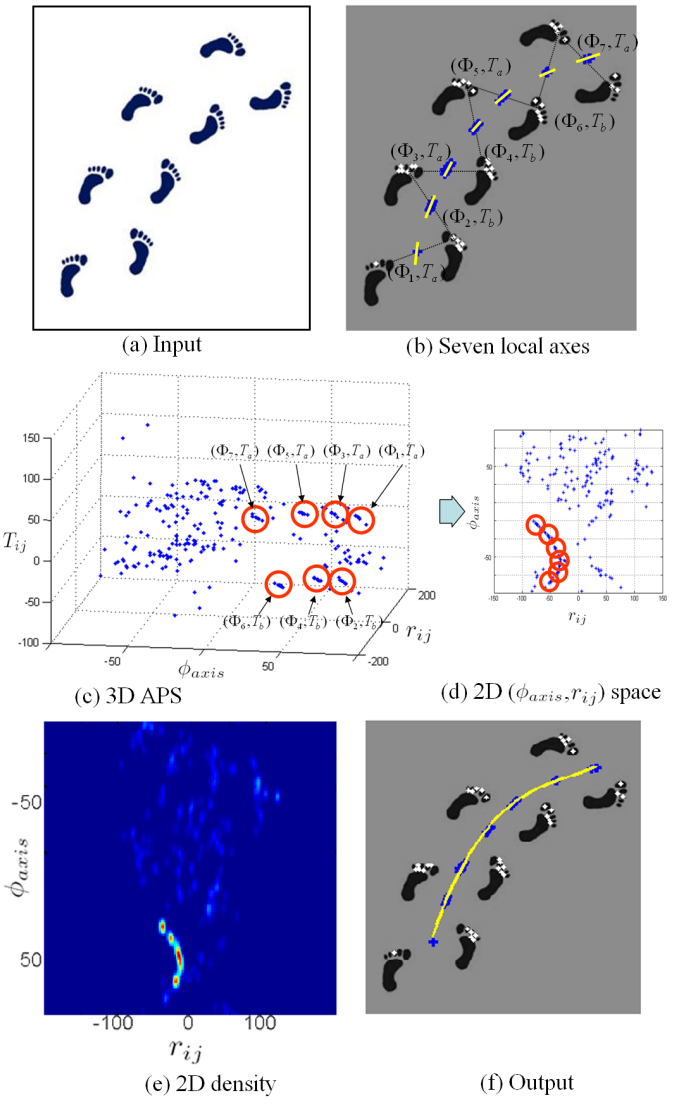

Fig. 10. An example of curved glide-reflection axis (cases (5) and (6) in Figure 4) detection: Blue points in (b) are center points of supporting matched pairs for each local axis. Yellow lines are local axes. 3D APS (c) shows each detected local axis (red circled). They have two different types of translation components (T_a and T_b), which are shown in (b).

V. Curved Glide-Reflection Axis Estimation

From an unsegmented image, without any previous knowledge, we need to extract potential local feature points that may lead to corresponding matches for glide-reflection symmetry. When the glide-reflection axis is curved, the axis does not appear as a single point in the APS voting space (Figure 9 (4)), as it does for the straight axis case (Figure 9 (1),(2)). A curved axis can be considered as a sequence of straight glide-reflection axes having different yet smoothly varying orientations with different glides (translations) T. Therefore, a curved axis can be estimated by fitting a curve to a set of contiguous points in the 3D APS. Based on the detected local glide-reflection matches, our algorithm seeks a set of local axes supporting a curved glide-reflection symmetry.

A. Grouping in a 3D APS

In real world images, multiple local straight glide-reflection axes of different orientations and translations form a single curved glide-reflection. Figure 10 (b) shows seven local axes (yellow lines) supporting a curved axis that is detected by our algorithm (Figure 10 (f)). We find the seven local maximum points on this 3D APS density (Figure 10 (c)). Each red circled set of matching pairs in Figure 10 (c) corresponds to a local axis shown in 10 (b). Note that they have two different types of translation components (T_a and T_b), which can be clearly detected in our 3D APS (Figure 10 (c)). Local axes close to each other with respect to the Euclidean distance of (r_{ij}, ϕ_{axis}) coordinate are connected. This can be done in a 2D density plot (Figure 10 (d)) obtained by accumulating points along the T-axis of the 3D APS density. Note that the distance between 90 and -90 in the ϕ_{axis} axis is considered to be zero. As a result, we find a series of straight local axes having contiguous r_{ij} and ϕ_{axis} values. Figure 10 (e) shows detected axes corresponding to a curved glide reflection axis in Figure 10 (f). After a set of connected axes are detected representing a global curved glide-reflection axis, we eliminate them from the 3D APS and repeat the grouping to detect the next curved glide-reflection axis.

B. Curve Fitting

Given all local axes detected in the 3D APS supporting a curved glide reflection axis, we can locate the center points m_k (blue points in Figure 10 (b)) of all supporting feature point pairs of the local axes back in the spatial domain. White points in Figure 10 (b) represent the feature point pairs supporting the selected axes. By connecting all center points, we can get a curved glide-reflection axis. However, the detected center points are not necessarily dense enough to find the correct glide-reflection axis. To achieve a smooth and precise curved axis, we apply a polynomial curve fitting given the center point set m_k. Based on an assumption that a curved axis can be approximated by a polynomial curve, we use polynomial curves $f_c(x) = a_0 + \sum_{i=1}^{c} a_i x^i$. We set c range from 1 to 5 in our experiments. Each degree of the polynomial is fit on a rotated input image I_j to find the best fit (rotation angles are $j = 0^o$, 45^o, 90^o and 135^o, respectively). We calculate the summation of distance $S(I_j, f_c(x)) = \sum_{k=1}^{N} d(k)$ where $d(k)$ is the distance from the computed center points m_k of an input image I_j to the polynomial $f_c(x)$. Among the total of 20 polynomial curves (5 polynomial degrees $\times$ 4 rotation angles), the one having the lowest distance S from all center points is selected as the final curved axis $f_{c_{fit}}(x)$ on $I_{j_{fit}}$, where $((j_{fit}, c_{fit}) = \arg\min_{j,c} S(I_j, f_c(x)))$.

However, in practical applications this curve fitting method suffers from outliers of the center points m_k, causing significant axis detection errors in curve fitting. In order to remove outliers and find the best subset of center points modeling the curved glide-reflection axis, we propose a modified RANSAC algorithm [70]. Before we perform the curve fitting, we randomly choose a subset of center points. Because we do not know the exact target shape of the model of each axis, we have multiple polynomial models of degrees 1 to 5. We compute

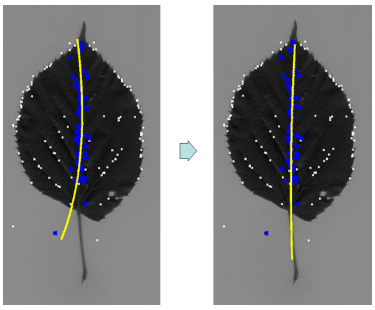

(a) Without RANSAC (b) With RANSAC

Fig. 11. Curve fitting with and without RANSAC (a) Outlier center point at the bottom left causes incorrect axis detection result. (b) RANSAC excludes the outlier and finds a better glide-reflection axis.

the squared sum of Euclidean distances from all points of the subset to each polynomial. Best fit with shortest distance among the polynomials is selected as a potential good model. Now we test with points outside of the subset to find a final good polynomial model. This step is repeated k times and the polynomial model with the lowest distance is chosen as the final polynomial curve fit on the axis. Pseudocode for this step is shown below:

Pseudocode of RANSAC algorithm for Curve Fitting

n is the smallest fraction of the number of m_k required
k is the number of iterations
t is the threshold used to decide whether a point fits well on the current curve
d is the fraction of the minimum number of center points required to be a good model (d>n)

```
For i=1 to i=k
        1. Draw a sample of n center points from the
        data uniformly and at random
        2. Fit polynomials to the subset and find
        the polynomial of the lowest distance
        3. For each point outside the subset
                Measure the distance to the polynomial
                If the distance is less than t, the point is close
        end
        If there are points in the subset with d or higher
        ratio, declare a good fit
        and calculate the current distance
        If current distance < minimum distance
                minimum distance = current distance
                best polynomial = current polynomial
end
Return best polynomial, minimum distance
```

Figure 11 demonstrates a polynomial curve fitting example with and without RANSAC. The detected curved axis in Figure 11 (a) is distorted by an outlier center point outside of the leaf at the bottom left side. RANSAC eliminates the outlier and finds the correct axis in Figure 11 (b).

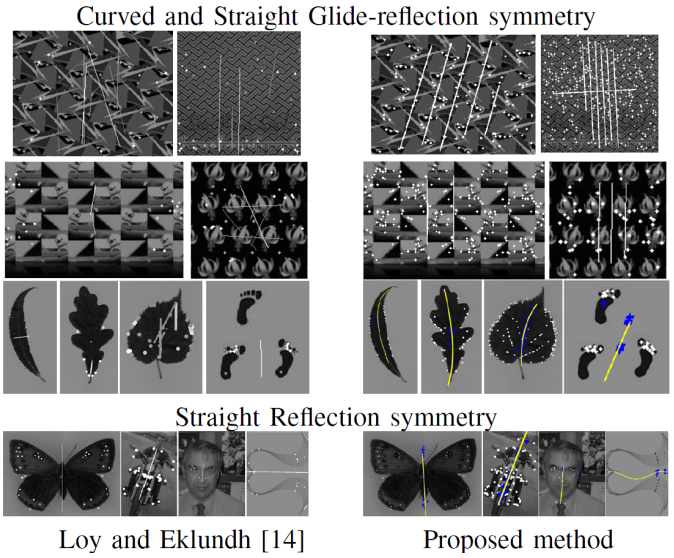

Fig. 13. Curved and straight glide-reflection axes detection comparison. Loy and Eklundh [15] detects no curved or straight glide-reflection axis. Several stronger glide-reflection axes in the middle of each wallpaper image are detected by the proposed method.

VI. Experimental Results

We test our algorithm on 64 images composed of reptile, insect, fish, human body, tiled-pattern, human face, butterfly, and spinal x-rays (Figure 12, 14, 13) and 1125 Swedish leaf images [71] (Figure 15). In our experiments, parameter values for the RANSAC algorithm are empirically assigned as follows: The smallest ratio of the number of center points required n is 0.3, the threshold used to decide that a point fits well on the current curve t is 25, the ratio of the minimum number of center points required to be a good model d is 0.9 and the iteration number k is 30.

Our method is coded in Matlab and runs on a Windows XP, 3.2GHz Pentium CPU. The processing time of the proposed algorithm mainly depends on the number of detected feature points, varying from hundreds to thousands. Detailed experimental results are presented below (the complete set of results are provided in our supplemental materials). Potential applications of the proposed algorithm are shown in Figures 16 and 17.

A. Curved Glide-Reflection Symmetry Detection in Real, Unsegmented Images

Table II shows the detection rates and mean processing time of the proposed algorithm compared to the reflection symmetry algorithm of [15] on the 64-test image set. For quantitative evaluation, we use the standard definition of true positive rate (sensitivity) defined as the number of detected symmetries over the number of the groundtruth (human identified). We also record the number of false positives. We consider it a false positive if our proposed method, with no pre-assumption of reflection symmetry types, fits a curved axis to a straight reflection axis due to a lack of detected center points m_k on the straight axis. On the other hand, Eklundh's algorithm [15] always try to find a straight reflection axis. We also compare

TABLE II

QUANTITATIVE EXPERIMENTAL RESULTS USING DIFFERENT IMAGE FILTERS, WITH AND WITHOUT RANSAC ON 64-TEST IMAGE SET

Method	**Detection Results - True Positive Rate % (# False Positives)**				**Processing time**
	Without filters/RANSAC	With RANSAC	With filters	With both filters/RANSAC	Average(std)
Proposed	75% (16)	77% (15)	77% (15)	80% (13)	9.7(10.3)sec
Loy and Eklundh [15]	31% (119)				6.1(9.4)sec

TABLE III

QUANTITATIVE EXPERIMENTAL RESULTS ON DIFFERENT TYPES OF REFLECTION SYMMETRY IMAGES ON THE 64-TEST IMAGE SET

Method	**Detection Results - True Positive Rate (# False Positive)**				
	Straight Reflection(21)	Straight Glide-Reflection(15)	Curved Reflection(18)	Curved Glide-Reflection(10)	Overall (64)
Proposed	86% (3)	80% (3)	83% (3)	60% (4)	80% (13)
Loy and Eklundh [15]	91% (9)	7% (46)	0% (38)	0% (26)	31% (119)

21, 15, 18 and 10 (64 total) test images are used for straight reflection, straight glide-reflection, curved reflection and curved glide-reflection, respectively. True positive rate (sensitivity) $= \frac{\#ofTP}{\#ofGT}$, GT = Ground Truth. False positive $= \#$ of False positives

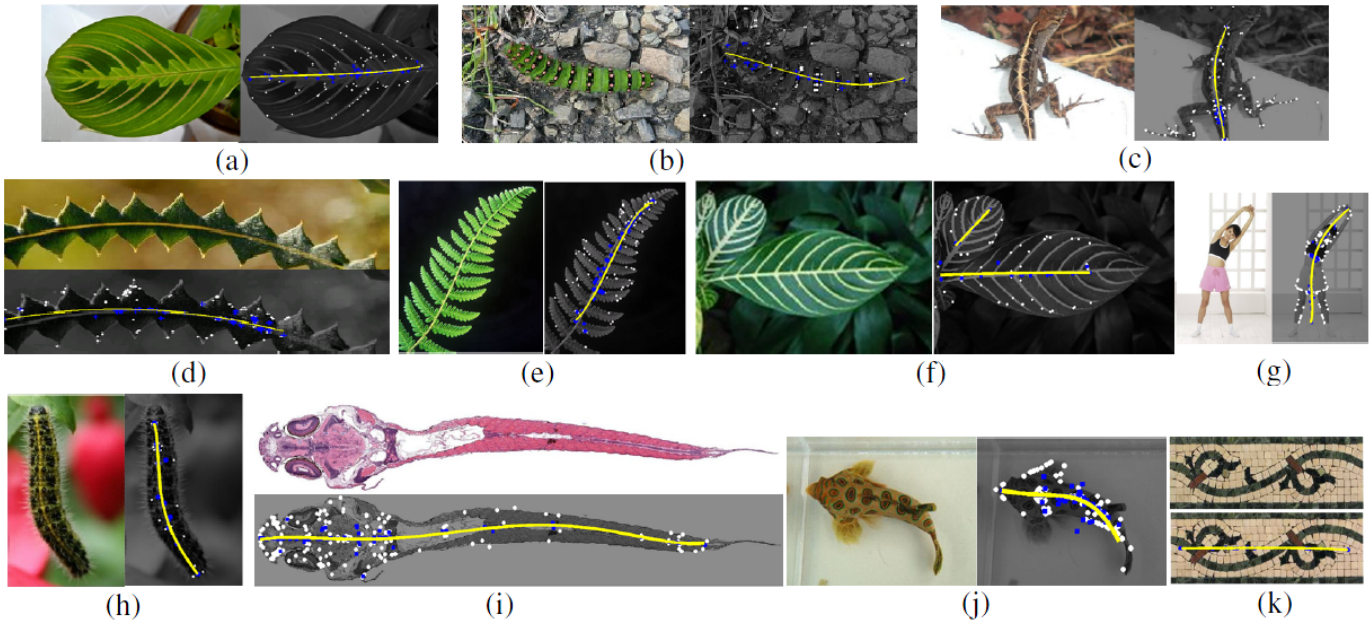

Fig. 12. Experimental results on real-world images. Two separate glide-reflection axes are found in (f).

the Current medial axes detection approaches (e.g. Peng et al [16]) is not designed to deal with the amount of clutter that is present in real world images, our evaluation results of [16] shows 0% sensitivity on the 64-test image set and a significantly longer time than the algorithms presented in Table II. Figure 12 shows some sample results of the proposed algorithm on real world images. Curved reflection symmetries are found on leaves or branches (Figure 12 (a), (d), (e) and (f)). Figure 12 (f) demonstrates that multiple curved glide-reflection symmetry axes can be detected in an image. Figure 12 (c) is a lizard with a reflection symmetry pattern on its back, which serves as a good example where the medial axis (extracted from its contour) and reflection axis (extracted from its texture pattern) differ. Figure 12 (i) is a stained pathology image of a zebra fish, where a curved reflection axis is supported by its interior features. The left part of the detected axis in Figure 12 (d) is inaccurate due to a center point outlier.

We further divide our 64-test image set into four subtypes: straight reflection, straight glide-reflection, curved reflection and curved glide-reflection symmetries and evaluate the algorithms performance respectively (Table III). Figure 13 shows some sample detection results of Loy and Eklundh's algorithm [15] versus our proposed algorithm.

Figure 14 (a) is a failure case, where the skewed pattern in the lower part of the ball is not correctly detected. In Figure 14 (b), background clutter results in many outliers that could not be completely removed by RANSAC. It also shows that polynomial curves may not be sufficient to capture the whole

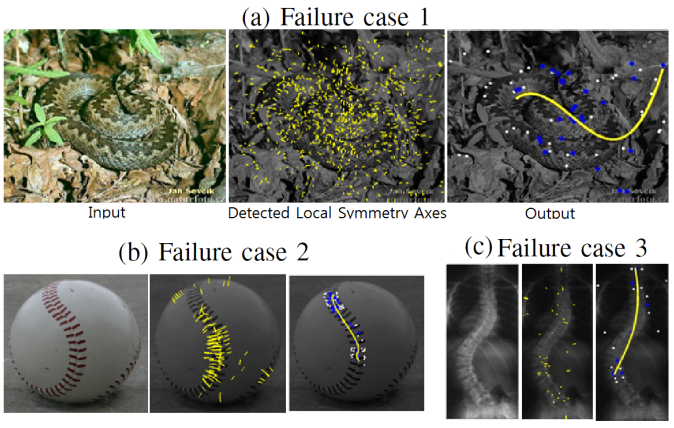

Fig. 14. Axis detection failure cases due to (a)background clutters (b)the skewed pattern in lower part and (c)the lack of key points.

curved axis. In Figure 14 (c), not enough key points are found to support the whole curved axis.

Figure 15 shows the detection results on the Swedish leaf classes from [71] that contain curved glide-reflection axes. Class 4 (Figure 15 (a)) has a weak texture pattern and challenging asymmetric contour shapes. Most leaves of Class 6 (Figure 15 (b)) have asymmetrical contour shapes where medial axis detection fails to detect the correct glide-reflection symmetry axes. Clear symmetric patterns on the leaves help our method to detect the correct curved axes. Class 10 has more complicated contours and patterns. Table IV summarizes the curved glide-reflection symmetry axis detection rate on all 15 classes of the Swedish leaf data set. The best detection rate is 65.3% of class 11 and the worst detection rate is 12.0% of class 7. Figure 15 (d) shows sample results of leaf axis detection failure. In most failure cases, lack of enough matched key point pairs causes the failure of correct and complete leaf axis detection.

B. Axis Curvature Estimation

One application of our algorithm is the detection of the curved spine axis from 2D x-ray images. Figure 17 (b) shows several curved spine axis detection results of the Scoliosis spine x-ray images. Our algorithm can detect the curvature of the spine automatically.

The curvature of a spine is an important cue for the diagnosis of Scoliosis disease. Cobb angle [72], a measurement that has been used for the evaluation of curves in Scoliosis, is an absolute angle difference of the two perpendicular lines at the two most tilted vertebrae to the horizontal line (Figure 16 left). Let $f(x)$ be a polynomial function representing the detected curved axis of a spine. We estimate the Cobb angle by taking a derivative of the detected curved axis and finding local maxima and minima points. Estimated Cobb angle $\hat{\theta}$ then can be computed as follows:

$$\hat{\theta} = \left| arctan(f^{'}(X_0^1)) - arctan(f^{'}(X_0^2)) \right| \qquad (5)$$

where X_0^1 and X_0^2 are two points where $f^{''}(x) = 0$. Figure 16 left shows automatic Cobb angle detection results from a spine image.

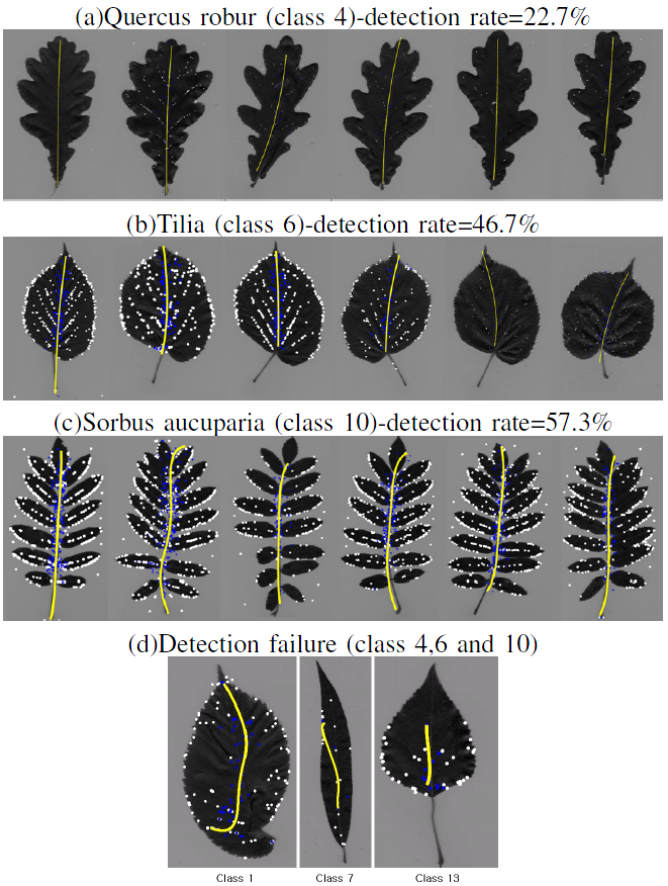

Fig. 15. Sample results of curved glide-reflection symmetry axis detection on the Swedish leaves [71] classes 1,7 and 13 respectively (Table IV). (d) Sample results of leaf axis detection failure from classes 4,6 and 10, respectively, due to failure of outlier elimination (class 1) or lack of enough center points detected (class 7 and 13).

C. Curved Axis Straightening

Once we find the curved glide-reflection axis with the parameterized axis model, we can calculate the curvature at any location on the curve. Based on the curvature information at each location, we can recover a straight axis by realigning each normal line of the curved axis vertically (Figure 16 right).

Figure 17 shows two examples of curved axis straightening. Some Swedish leaves [71] (Figure 17 (a)) have curved reflection axes. After automatic curved axis detection by the proposed algorithm we can straighten the original images. This process is a type of normalization process along the reflection axis for leaf image registration. Shape recognition methods for deformable objects can benefit from this quantification and normalization of the deformation for further discrimination of the shape. Figure 17(b) is another example using X-ray images of spines with Scoliosis disease from the previous section.

VII. Curved Glide-Reflection Surface Detection

Our proposed algorithm can also be applied to curved glide reflection surface detection based on a set of 2D slices. Local glide-reflection symmetries in each slice are detected and their center points are collected (Figure 18 (b)). We then perform a surface fitting [73] on the center points of the set of 2D

TABLE IV
SYMMETRY AXIS DETECTION FROM SWEDISH LEAF DATA [71]

Leaf - Classes	**Detection Rate**				
(15classes x 75samples = 1125leaves)	Loy and Eklundh [15]	Proposed Method			
		Neither	RANSAC Only	Filter Only	Filter+RANSAC
Ulmus carpinifolia (class 1)	5/75 = 6.7	18/75 = 24.0	18/75 = 24.0	21/75 = 28.0	21/75 = 28.0
Acer platanoides (class 2)	18/75 = 24.0	29/75 = 38.7	30/75 = 40.0	33/75 = 44.0	35/75 = 46.7
Ulmus (class 3)	4/75 = 5.3	32/75 = 42.7	32/75 = 42.7	36/75 = 48.0	39/75 = 52.0
Quercus robur (class 4)	5/75 = 6.7	3/75 = 4.0	3/75 = 4.0	17/75 = 22.7	17/75 = 22.7
Alnus incana (class 5)	10/75 = 13.3	28/75 = 37.3	28/75 = 37.3	31/75 = 41.3	31/75 = 41.3
Tilia (class 6)	9/75 = 12.0	20/75 = 26.7	21/75 = 28.0	33/75 = 44.0	35/75 = 46.7
Salix fragilis (class 7)	0/75 = 0.0	3/75 = 4.0	3/75 = 4.0	9/75 = 12.0	9/75 = 12.0
Populus tremula (class 8)	15/75 = 20.0	10/75 = 13.3	11/75 = 14.7	13/75 = 17.3	13/75 = 17.3
Corylus avellana (class 9)	3/75 = 4.0	20/75 = 26.7	25/75 = 33.3	26/75 = 34.7	32/75 = 42.7
Sorbus aucuparia (class 10)	9/75 = 12.0	32/75 = 42.7	32/75 = 42.7	40/75 = 53.3	43/75 = 57.3
Prunus padus (class 11)	2/75 = 2.7	31/75 = 41.3	31/75 = 41.3	49/75 = 65.3	49/75 = 65.3
Tilia 2 (class 12)	18/75 = 24.0	28/75 = 37.3	28/75 = 37.3	35/75 = 46.7	35/75 = 46.7
Populus (class 13)	10/75 = 13.3	30/75 = 40.0	31/75 = 41.3	35/75 = 46.7	35/75 = 46.7
Sorbus hybrida (class 14)	5/75 = 6.7	21/75 = 28.0	22/75 = 29.3	35/75 = 46.7	37/75 = 49.3
Fagus silvatica (class 15)	3/75 = 4.0	17/75 = 22.7	17/75 = 22.7	22/75 = 29.3	23/75 = 30.7
Average (Standard Deviation)	116/1125=10.3 (7.6)	322/1125=28.6 (13.2)	332/1125=29.5 (13.3)	435/1125=38.7 (14.4)	452/1125=40.2 (15.1)

The use of RANSAC and image filters improves the detection rate (Figure 7).

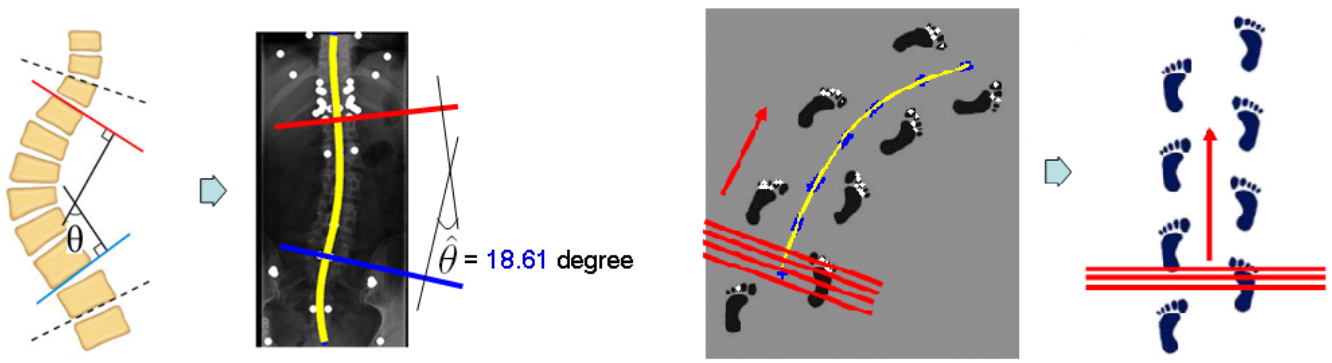

Fig. 16. Left: Cobb angle estimation by taking a derivative of the detected curved axis, Right: Curved axis straightening

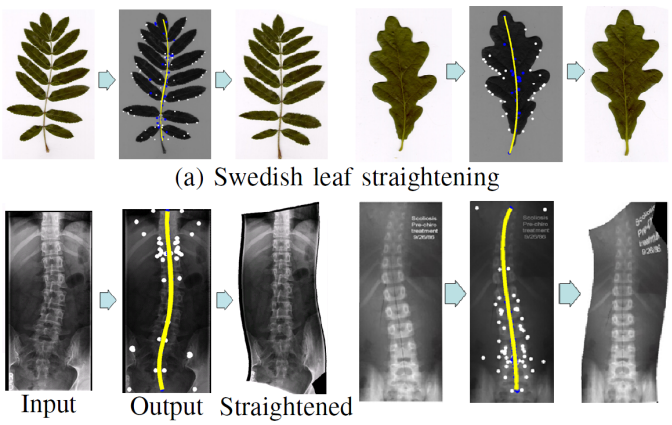

(a) Swedish leaf straightening

(b) Scoliosis spine straightening

Fig. 17. Curved axis straightening on (a) Swedish leaves and (b) Scoliosis spines.

slices in 3D space instead of polynomial curve fitting in 2D to find a curved glide-reflection surface. All slices are stacked along the Z-axis. We select one of the two 2D planes (X-Z and Y-Z planes) by taking the plane having higher variance of point locations projected onto each plane ((x_i, z_i) or (y_i, z_i)). Let us assume that the X-Z plane has a higher variance, as is the case in Figure 18 (b), then the curved surface function that we are fitting on the center points can be represented as $y_i = f(x_i, z_i)$, where $i \in [1, K]$ and K is the # of center points from all slices. The X-Z plane is now divided into multiple grids uniformly and a spline-based surface fitting method [73] is applied. We do a bilinear interpolation and gradient-based smoothing at each point to get a curved surface.

We have applied our method to two types of volumetric data with approximate bilateral symmetry plane. The zebrafish atlas [74] (Figure 18 (a)) is a set of 3D scan slice images of a zebrafish. Figure 18 (c) is the surface fitting result

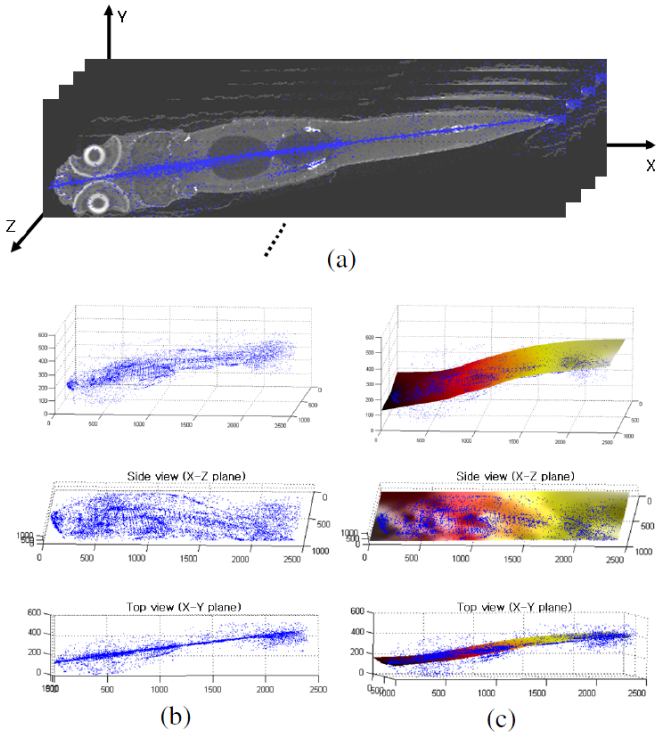

Fig. 18. Curved reflection surface detection on 3D CT images of zebrafish: (a)A set of 2D slices of a 3D Zebrafish (b)Detected center points (blue dots) of glide-reflection symmetries in data space (c)3D Surface fitting

of a zebrafish. Figure 19 show mid-sagittal surfaces of the human brain, detected from MR image stacks. The mid-sagittal surface of a brain with tumor is also correctly detected based on the overall bilateral structure of the brain.

For a general extension of the proposed method to 3D curved glide-reflection axis detection rather than the extension of 2D algorithm to curved reflection surface detection in 3D images, the SIFT keypoint detector would have to be replaced by a robust 3D feature point detector and 3D feature orientation estimator, and the dimensions of the axis parameter space would have to be extended.

VIII. Conclusion

We generalize the concept of reflection symmetry to curved glide-reflection symmetries that are common in the real world, especially in biomedical image data. The main contribution of this work is a formalization of curved glide reflection symmetry and its six sub-cases. The most popular straight reflection symmetry in computer and human vision applications thus far becomes one of its six cases. We also propose a feasible algorithm to detect a curved glide-reflection symmetry axis based on local feature extraction and parameter subspace matching. Our analysis provides both theoretical completeness of the formalization and practical guidance for our proposed algorithm. The proposed algorithm can deal with globally and locally skewed curved glide-reflection symmetries as long as the extracted features are affine or perspective invariant. We have evaluated our algorithm using a diverse image test set (64 images) of curved and straight reflection axes (Tables II and III), achieving an average 80% success rate (Table II). Furthermore, a quantitative comparison study on more than 1,000 leaf images shows superior performance of our proposed algorithm over a state of the art straight reflection symmetry axis detection algorithm [15] (Table IV). The proposed algorithm has an $O(N_f^2)$ complexity where N_f is the number of feature points extracted. Our proposed algorithm is also applied to 3-dimensional data to detect a curved glide-reflection symmetry surface such as the mid-sagittal surface of a human brain (normal or with tumor) or of the whole body micro-CT image of a zebrafish.

Though the proposed algorithm shows promise, there is plenty of room for improvement. First of all, like all feature-based methods, the performance of our algorithm suffers if the feature point extraction step fails to generate sufficient number of relevant feature points. For example, input images with smooth, clean contours and no texture (roughly speaking, images containing purely shape information with no appearance information) may not yield good results due to a lack of SIFT-like features. A quantitative evaluation of the difference between (SIFT) feature-based and region-based symmetry detection methods can be found in [75]. Since we have observed a detection rate increase (41.3% $\rightarrow$ 65.3% with class 11) in Table IV given an increase in filter diversity, we believe an even more versatile interest-point extractor may prove to be effective. Second, the grouping method in our 3D axis parameter space (APS) favors bigger and longer curved axes supported by more feature point pairs (e.g. Figure 12 (k)). This strategy occasionally eliminates small, weak, but true curved reflection symmetries. It is possible that a hierarchical approach can be adopted to address this problem. Finally, a better regression method like spline curve fitting can improve the curve fitting performance for real images containing complicated curved axes in cluttered backgrounds, like the snake example in Figure 14 (b). We can also further extend the curve fitting procedure to closed-contour for circle or ellipse fitting. For computer vision applications, the outcome of our proposed algorithm can be used for saliency detection, curvature or abnormality quantification and ultimately for object detection and recognition in unsegmented real world images.

Acknowledgment

The authors would like to thank Loy and Eklundh [15] and Peng et al. [16] for their respective source code, and Dr. K. C. Cheng for the zebrafish images. This work is supported in part by a PSU CTSA grant and a Northrop Grumman Gift grant to the last author.

References

[1] P. Locher and C. Nodine, "Symmetry catches the eye," *Eye Movements: from Physiology to Cognition, O'Regan, J. and Levy-Schoen, A., Elsevier Science Publishers B.V.*, 1987.

[2] G. Kootstra, A. Nederveen, and B. de Boer, "Paying attention to symmetry," *Proceedings of the British Machine Vision Conference (BMVC2008)*, pp. 1115–1125, September 2008.

[3] G. Heidemann, "Focus-of-attention from local color symmetries," *IEEE Trans. Pattern Anal. Mach. Intell.*, vol. 26, no. 7, pp. 817–830, 2004.

[4] D. Reisfeld, H. Wolfson, and Y. Yeshurun, "Context free attentional operators: The generalized symmetry transform," *International Journal of Computer Vision*, vol. 14, pp. 119–130, 1995.

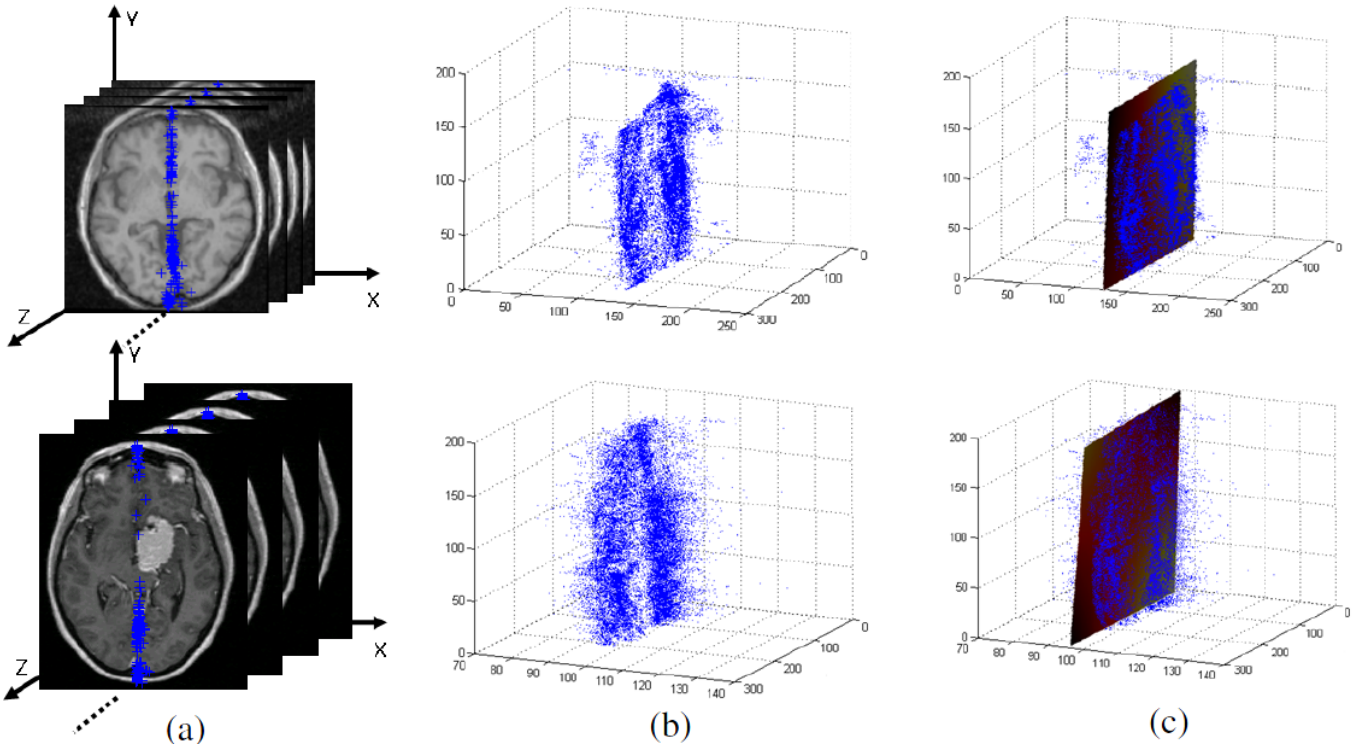

Fig. 19. Mid-sagittal surface detection on 3D human brain with(right) and without(left) tumor of significant size using proposed curved glide-reflection symmetry detection method: (a)A set of 2D slices of a 3D brain (b)Detected center points (blue dots) of glide-reflection symmetries in data space (c)3D Surface fitting

[5] Y. Liu, H. Hel-Or, C. S. Kaplan, and L. V. Gool, "Computational symmetry in computer vision and computer graphics," *Foundations and Trends in Computer Graphics and Vision*, vol. 5, pp. 1–195, 2010.

[6] H. Weyl, *Symmetry*. Princeton University Press, 1952, iSBN 0-691-02374-3.

[7] T. J. Christopher, *Compactifications Of Symmetric Spaces*. Birkhauser, 1997, iSBN 0817638997.

[8] S. Mitra and Y. Liu, "Local facial asymmetry for expression classification," in *Proceedings of International Conference on Computer Vision and Pattern Recognition*, vol. 2, June 2004, pp. 889 – 894.

[9] A. Kuehnle, "Symmetry-based recognition of vehicle rears," *Pattern Recogn. Lett.*, vol. 12, no. 4, pp. 249–258, 1991.

[10] B. Dai, Y. Fu, and T. Wu, "A vehicle detection method via symmetry in multi-scale windows," in *2nd IEEE Conference on Industrial Electronics and Applications*, May 2007, pp. 1827–1831.

[11] M. Mancas, B. Gosselin, and B. Macq, "Fast and automatic tumoral area localisation using symmetry," *IEEE International Conference on Acoustics, Speech, and Signal Processing.*, vol. 2, pp. 725–728, 18-23, 2005.

[12] X. Yang, J. Pei, and W. Xie, "Rotation registration of medical images based on image symmetry," in *Advances in Intelligent Computing*, vol. 3644, May 2005, pp. 68–76.

[13] Y. Liu, R. Collins, and W. E. Rothfus, "Robust midsagittal plane extraction from normal and pathological 3d neuroradiology images," *IEEE Transactions on Medical Imaging*, vol. 20, no. 1, pp. 175 – 192, 2001.

[14] Y. Liu, R. Collins, and Y. Tsin, "A computational model for periodic patern perception based on frieze and wallpaper groups," *IEEE Transactions on Pattern Analysis and Machine Intelligence*, vol. 26, no. 3, pp. 354–371, 2004.

[15] G. Loy and J. Eklundh, "Detecting symmetry and symmetric constellations of features," in *European Conference on Computer Vision*, 2006, pp. II: 508–521.

[16] H. Peng, F. Long, X. Liu, S. K. Kim, and E. W. Myers, "Straightening c. elegans images," *Bioinformatics*, pp. btm569+, November 2007.

[17] G. D. Birkoff and O. D. Kellogg, "Aesthetic measure," *Cambridge*, 1932.

[18] T. Kanade, "Recovery of the three-dimensional shape of an object from a single view," *Artificial Intelligence*, vol. 17, pp. 409–460, 1981.

[19] J. Wolter, T. Woo, and R. Volz, "Optimal algorithms for symmetry detection in two and three dimensions," *Visual Computer*, vol. 1, pp. 37–48, 1985.

[20] G. Marola, "On the detection of the axes of symmetry of symmetric and almost symmetric planar images," *IEEE Transactions on Pattern Analysis and Machine Intelligence*, vol. 11, no. 1, pp. 104–108, January 1989.

[21] P. Saint-marc and G. Medioni, "B-spline contour representation and symetry detection." European Conference on Computer Vision (ECCV), 1990, pp. 604–606.

[22] J. Ponce, "On characterizing ribbons and finding skewed symmetries," *Comput. Vision Graph. Image Process.*, vol. 52, pp. 328–340, October 1990.

[23] Y. Liu, "Symmetry groups in robotic assembly planning," in *doctoral dissertation, University of Massachusetts Amherst*, September 1990.

[24] T. Zielke, M. Brauckmann, and W. Seelen, "Intensity and edge-based symmetry detection applied to car-following." European Conference on Computer Vision (ECCV), 1992, pp. 865–873.

[25] F. Labonte, Y. Shapira, and P. Cohen, "A perceptually plausible model for global symmetry detection," in *Computer Vision, 1993. Proceedings., Fourth International Conference on*, May 1993, pp. 258–263.

[26] Y. Liu and R. Popplestone, "A group theoretic formalization of surface contact," *International Journal of Robotics Research*, vol. 13, no. 1, pp. 148–161, April 1994.

[27] H. Zabrodsky, S. Peleg, and D. Avnir, "Symmetry as a continuous feature," *IEEE Transactions on Pattern Analysis and Machine Intelligence*, vol. 17, no. 12, pp. 1154–1166, 1995.

[28] D. P. Mukherjee, A. Zisserman, and M. Brady, "Shape from symmetry: Detecting and exploiting symmetry in affine images," *Philosophical Transactions: Physical Sciences and Engineering*, vol. 351, no. 1695, pp. 77–106, 1995. [Online]. Available: http://www.jstor.org/stable/54462

[29] L. Van Gool, M. Proesmans, and T. Moons, "Mirror and point symmetry under perspective skewing," in *Proceedings of International Conference on Computer Vision and Pattern Recognition*, 1996, pp. 285–292.

[30] Y. Sato and S. Tamura, "Detecting planar and curved symmetries of 3d shapes from a range image," *Computer Vision and Image Understanding*, vol. 64, no. 1, pp. 175–187, 1996.

[31] A. Tuzikov, G. Margolin, and A. Grenov, "Convex set symmetry measurement via minkowski addition," *Journal of Mathematical Imaging and Vision*, vol. 7, no. 1, pp. 53–68, January 1997.

[32] C. Sun and J. Sherrah, "3-d symmetry detection using the extended gaussian image," *IEEE Transactions on Pattern Analysis and Machine Intelligence*, vol. 19, pp. 164–168, 1997.
[33] N. Kiryati and Y. Gofman, "Detecting symmetry in grey level images: The global optimization approach," *Int Journal of Computer Vision*, vol. 29, no. 1, pp. 29–45, 1998.
[34] S. Carlsson, "Symmetry in perspective," in *European Conference on Computer Vision vol.1*, 1998, pp. 249–263.
[35] R. Curwen, J. Mundy, and C. Stewart, "Recognition of plane projective symmetry,." ICCV, 1998, pp. 1115–1122.
[36] A. M. Bruckstein and D. Snaked, "Skew symmetry detection via invariant signatures," *Pattern Recognition*, vol. 31, no. 2, 1998.
[37] C. Sun and D. Si, "Fast reflectional symmetry detection using orientation histograms," *Real-Time Imaging*, vol. 5, no. 1, pp. 63–74, 1999.
[38] Y. Lei and K. Wong, "Detection and localisation of reflectional and rotational symmetry under weak perspective projection," *Pattern Recognition*, vol. 32, no. 2, pp. 167–180, 1999.
[39] D. Shen, H. Ip, and E. Teoh, "Robust detection of skewed symmetries," in *International Conference on Pattern Recognition*, 2000, pp. 1010–1013.
[40] M. Kazhdan, B. Chazelle, D. Dobkin, A. Finkelstein, and T. Funkhouser, "A reflective symmetry descriptor," in *European Conference on Computer Vision (ECCV*, 2002, pp. 642–656.
[41] V. Prasad and B. Yegnanarayana, "Finding axes of symmetry from potential fields," *IEEE Transactions on Image Processing*, vol. 13, no. 12, pp. 1559–1566, Dec. 2004.
[42] T. Yuan and X. Tang, "Efficient local reflectional symmetries detection," in *IEEE International Conference on Image Processing*, vol. 3, Sept. 2005, pp. III–1180–3.
[43] G.Marola, "A technique for finding the symmetry axes of implicit polynomial curves under perspective projection," *IEEE Transactions on Pattern Analysis and Machine Intelligence*, vol. 27, no. 3, pp. 465–470, March 2005.
[44] Y.-Q. X. Yanxi Liu, James H. Hays and H.-Y. Shum, "Digital papercutting," in *Technical Sketch, SIGGRAPH*, 2005.
[45] H. Cornelius and G. Loy, "Detecting bilateral symmetry in perspective," in *Proceedings of International Conference on Computer Vision and Pattern Recognition Workshop*, 2006, p. 191.
[46] N. J. Mitra, L. J. Guibas, and M. Pauly, "Partial and approximate symmetry detection for 3d geometry," *ACM Trans. Graph.*, vol. 25, no. 3, pp. 560–568, 2006.
[47] A. Martinet, C. Soler, N. Holzschuch, and F. X. Sillion, "Accurate detection of symmetries in 3d shapes," *ACM Trans. Graph.*, vol. 25, no. 2, pp. 439–464, 2006.
[48] J. Podolak, P. Shilane, A. Golovinskiy, S. Rusinkiewicz, and T. Funkhouser, "A planar-reflective symmetry transform for 3d shapes," *ACM Transactions on Graphics (Proc. SIGGRAPH)*, vol. 25, no. 3, Jul. 2006.
[49] N. J. Mitra, L. Guibas, and M. Pauly, "Symmetrization," in *ACM Transactions on Graphics*, vol. 26, no. 3, 2007, pp. #63, 1–8.
[50] K. Bitsakos, H. Yi, L. Yi, and C. Fermuller, "Bilateral symmetry of object silhouettes under perspective projection," in *ICPR08*, 2008, pp. 1–4.
[51] M. Pauly, N. J. Mitra, J. Wallner, H. Pottmann, and L. Guibas, "Discovering structural regularity in 3D geometry," *ACM Transactions on Graphics*, vol. 27, no. 3, pp. #43, 1–11, 2008.
[52] T. Riklin-Raviv, N. Sochen, and N. Kiryati, "On symmetry, perspectivity, and level-set-based segmentation," *IEEE Trans. Pattern Anal. Mach. Intell.*, vol. 31, pp. 1458–1471, August 2009.
[53] J. Liu and Y. Liu, "Curved reflection symmetry detection with self-validation." ACCV, 2010.
[54] A. Ylä-Jääski and F. Ade, "Grouping symmetrical structures for object segmentation and description," *Comput. Vis. Image Underst.*, vol. 63, pp. 399–417, May 1996.
[55] V. Prasad and L. Davis, "Detecting rotational symmetries," in *Proceedings of IEEE International Conference on Computer Vision*, 2005, pp. 954–961.
[56] P.-C. Chen, J. H. Hays, S. Lee, M. Park, and Y. Liu, "A quantitative evaluation of symmetry detection algorithms," Robotics Institute, Pittsburgh, PA, Tech. Rep. CMU-RI-TR-07-36, September 2007.
[57] D. Milner, S. Raz, H. Hel-Or, D. Keren, and E. Nevo, "A new measure of symmetry and its application to classification of bifurcating structures," *Pattern Recogn.*, vol. 40, pp. 2237–2250, August 2007.
[58] D. A. Forsyth and J. Ponce, *Computer Vision: A Modern Approach*. Prentice Hall, August 2002.
[59] M. Brady and H. Asada, "Smoothed local symmetries and their implementation," Tech. Rep., MIT, 1984.
[60] K. Siddiqi and e. S. Pizer, "Medial representations: Mathematics, algorithms and applications," *Springer, Series: Computational Imaging and Vision*, vol. 37, 2008.
[61] A. Levinshtein, S. Dickinson, and C. Sminchisescu, "Multiscale symmetric part detection and grouping," in *IEEE International Conference on Computer Vision*, Sep 2009.
[62] R. Guillemaud, P. Marais, A. Zisserman, B. McDonald, T. Crow, and M. Brady, "A three dimensional mid sagittal plane for brain asymmetry measurement," *Schizophr*, vol. 18, pp. 183–184, 1996.
[63] Y. Liu and R. Collins, "Automatic extraction of the central symmetry plane from neuroradiology images," Robotics Institute, Pittsburgh, PA, Tech. Rep. CMU-RI-TR-96-40, December 1996.
[64] Y. Liu, R. Collins, and W. E.Rothfus, "Evaluation of a robust midsagittal plane extraction algorithm for coarse, pathological 3d images," in *Proceedings of the Medical Imaging Computing and Computer Assisted Intervention Conference (MICCAI 2000)*, Pittsburgh, PA, October 2000.
[65] B. Ardekani, J. Kershaw, M. Braun, and I. Kanno, "Automatic detection of the mid-sagittal plane in 3-d brain images," *IEEE Transactions on Medical Imaging*, vol. 16, pp. 947–952, 1997.
[66] S. Minoshima, K. L. Berger, K. S. Lee, and M. A. Mintum, "An automated method for rotational correction and centering of three-dimensional functional brain images," *European Journal of Nuclear Medicine and Molecular Imaging*, vol. 33, pp. 1579–1585, 1992.
[67] S. Prima, S. Ourselin, and N. Ayache, "Computation of the mid-sagittal plane in 3-d images," in *IEEE Transactions on Medical Imaging*, vol. 21, 2002, pp. 122–138.
[68] M. B. Stegmanna, K. Skoglunda, and C. Rybergb, "Mid-sagittal plane and mid-sagittal surface optimization in brain mri using a local symmetry measure," *Medical Imaging*, vol. 5747, pp. 568–579, 2005.
[69] D. G. Lowe, "Distinctive image features from scale-invariant keypoints," *International Journal of Computer Vision*, vol. 60, pp. 91–110, 2004.
[70] M. A. Fischler and R. C. Bolles, "Random sample consensus: a paradigm for model fitting with applications to image analysis and automated cartography," *Readings in computer vision: issues, problems, principles, and paradigms*, pp. 726–740, 1987.
[71] O. J. O. Söderkvist, "Computer vision classification of leaves from swedish trees," Master's thesis, Linköping University, SE-581 83 Linköping, Sweden, September 2001, liTH-ISY-EX-3132.
[72] G. D. Birkoff and O. D. Kellogg, "Outline for the study of scoliosis," *AAOS Instructional Course Lectures*, pp. 261–275, 1948.
[73] J. DErrico, "Surface fitting using gridfit," *MATLAB Central File Exchange*, Retrieved Jul 01, 2009.
[74] *Zebrafish Atlas, http://zfatlas.psu.edu/index.php*.
[75] S. Lee and Y. Liu, "Skewed rotation symmetry group detection," *IEEE Transactions on Pattern Analysis and Machine Intelligence (PAMI)*, vol. 31, pp. 1458–1471, September 2010.

Seungkyu Lee received the BS and MS degrees in electrical engineering from Korea Advanced Institute of Science and Technology, Daejeon, South Korea, in 1997 and 1999, respectively, and Ph.D in computer science & engineering from The Pennsylvania State University in 2009. He is currently a principal research engineer in Samsung advance institute of Technology. His current research interests include symmetry feature detection and 3D scene reconstruction. He is a member of the IEEE and the IEEE Computer Society.

Yanxi Liu received the BS degree in physics/electrical engineering from Beijing, China, the PhD degree in computer science for group theory applications in robotics from the University of Massachusetts, Amherst, and postdoctoral training at LIFIA/IMAG, Grenoble, France. She also spent one year at the US National Science Foundation (NSF) Center for Discrete Mathematics and Theoretical Computer Science (DIMACS) with an NSF Research Education Fellowship Award, and a sabbatical-semester in the radiology department of UPMC. She serves as the co-director of the Lab for Perception, Action, and Cognition (LPAC) and is a tenured faculty member of the Computer Science Engineering and Electrical Engineering Departments of The Pennsylvania State University. Before joining PSU, Dr. Liu was an associate research professor in the Robotics Institute of Carnegie Mellon University. Her research interests span a wide range of applications, including computer vision, computer graphics, robotics, human perception, and computer-aided diagnosis in medicine, with a theme on computational symmetry/regularity and discriminative subspace learning from large, multimedia datasets. She co-chaired the International Workshop on ”Computer Vision in Biomedical Image Applications” (ICCV 2005), and is chairing the first US NSF funded international competition on ”Symmetry Detection from Real World Images” (CVPR 2011). She is a senior member of the IEEE and the IEEE Computer Society.